

## Absolute cross sections for electron-impact ionization of the rare-gas atoms by the fast-neutral-beam method

Robert C. Wetzel, Frank A. Baiocchi, Todd R. Hayes, and Robert S. Freund

*AT&T Bell Laboratories, Murray Hill, New Jersey 07974*

(Received 23 July 1986)

A new apparatus has been constructed for the measurement of absolute partial electron-impact ionization cross sections of neutral atoms, molecules, and free radicals. A fast neutral beam is prepared by charge-transfer neutralization of a mass-selected ion beam and is ionized as it crosses an electron beam. From careful analysis of the apparatus, the absolute accuracy of measured cross sections is calculated to be  $\pm 12\%$ . Combined with statistical errors, this gives about  $\pm 15\%$  for the overall accuracy. Measurements of ionization cross sections for the four rare gases He, Ne, Ar, and Kr from 0 to 200 eV agree with the most reliable previous values within  $\pm 6\%$ . The measured Xe ionization cross section is 12% greater than the previous best value. Ratios of double- and triple-ionization to single-ionization cross sections for Ar, Kr, and Xe confirm the recent measurements of Stephan, Helm, and Märk [J. Chem. Phys. 73, 3763 (1980)].

### I. INTRODUCTION

Although absolute cross sections for ionization by electron impact are of fundamental and widespread importance, relatively little quantitative and reliable information is available. Almost all measurements of neutral species have been limited to stable gases or vapors, primarily about three dozen atoms and simple molecules. Only a few of these measurements have separated product ions by fragment species or charge state.

Several methods have been introduced recently which permit accurate, absolute measurements with full separation and identification of the product species.<sup>1</sup> We have chosen to further develop one of these methods, one in which a fast neutral beam is crossed by an electron beam.<sup>2-7</sup> It is capable of quantitative measurements of molecular fragment cross sections as well as of parent species, and of unstable atomic and molecular parents (such as free radicals and metastable states) as well as of stable atoms and molecules. Several preliminary reports have been published.<sup>8-11</sup> The purpose of this paper is to present the apparatus, the procedures, the accuracy tests, and the error estimates. As verification of the overall procedure, we remeasure cross sections for the rare-gas atoms from threshold to 200 eV.

The rare-gas-atom ionization cross sections have been measured many times (as reviewed in Refs. 1, 12, and 13), but only a few of those measurements are absolute, that is, with no normalization to previous experiments or to theory. Most of those absolute measurements are of the total cross section  $\sigma_T$ , that is, with no separation of charge states. One of the earliest measurements was for He, Ne, and Ar by Smith in 1930.<sup>14</sup> This work remained the standard until 1965 when Rapp and Englander-Golden<sup>15</sup> (REG) carefully repeated the measurements, paying special attention to systematic errors. To their results for  $\sigma_T$ , which have now become the standards, they assign an uncertainty of  $\pm 7\%$ . The only absolute measurements of total cross sections in the low-energy range

since those of REG are those of Kurepa *et al.*<sup>16</sup> for Ar to an estimated error of 5%, and of Fletcher and Cowling<sup>17</sup> for Ne and Ar to an estimated error of 4%. (The measurements of Nagy *et al.*<sup>18</sup> begin at 500 eV and so do not overlap the energy range of our measurements.) More recently, Montague, Harrison, and Smith<sup>19</sup> have used the crossed-beam method to measure the absolute partial cross section for ionization of He to He<sup>+</sup>. Their value is directly comparable to that of REG's total cross section because the partial cross section for ionization to He<sup>2+</sup> is so small.<sup>20</sup> They report an uncertainty of  $\pm 4\%$  and a value which agrees with REG to that accuracy, inspiring confidence in both measurements. Thus, for He, there are only two independent and reliable absolute measurements below 200 eV, two such measurements for Ne, three for Ar, one for Kr, and one for Xe. Only the measurements of REG include all five rare gases.

Märk and co-workers<sup>20-22</sup> have made careful measurements of the relative partial cross sections for the rare gases He through Xe in the low-electron-energy regime (below 200 eV). They included careful measurements of the cross-section ratios for multiple to single ionization. From these measurements and appropriate weighting by charge, they constructed relative total ionization cross sections which agree in shape with those of REG to better than a few percent. They then used this comparison to normalize their relative measurements.

### II. APPARATUS

The crossed fast-neutral-beam—electron-beam method has been discussed several times in the literature.<sup>3-8</sup> Briefly (see Fig. 1), a fast beam of ions (3 keV) is formed, mass filtered, and then neutralized by symmetric charge transfer. The resulting beam of fast neutral atoms maintains the collimation of the ion beam. The flux of neutral atoms is measured absolutely with a calibrated detector. The ionization cross-section measurement is made by crossing the neutral beam with a well-characterized elec-

tron beam. The resulting ion beam is then focused by an einzel lens, separated into different charge states with a hemispherical electrostatic analyzer, and counted with a channel electron multiplier (CEM). Although use of the einzel lens and hemispherical analyzer introduces more complication than the minimum required for these measurements on atoms, it is crucial for experiments on molecules, where 100% collection of fragment ions is more difficult.

The ionization cross section  $\sigma(E)$  is given for this crossed-beam configuration by an expression from Kieffer and Dunn<sup>12</sup>

$$\sigma(E) = \frac{I_i(E)v_n v_e}{I_e(E)RF(v_e^2 + v_n^2)^{1/2}}, \quad (1)$$

where  $I_i(E)$  and  $I_e(E)$  are the ion and electron currents, respectively,  $v_n$  and  $v_e$  are the neutral and electron-beam velocities, respectively,  $R$  is the neutral-beam flux (atoms/sec), and  $F$  is a measure of the overlap between the neutral and electron beams:

$$F = \frac{\int j_n(z)j_e(z)dz}{\int j_n(z)dz \int j_e(z)dz}, \quad (2)$$

where  $j_n$  and  $j_e$  are spatial distributions of the neutral and electron beams, respectively. Thus an absolute measurement of  $\sigma(E)$  consists of measuring each of the quantities  $I_i(E)$ ,  $I_e(E)$ ,  $R$ ,  $F$ , and  $v_n$  without normalizing to previous experiments or theory.

Many of the pitfalls and potential systematic errors which occur in making an absolute measurement have been discussed by Kieffer and Dunn.<sup>12</sup> We address these and additional sources of error below.

## A. The neutral beam

### 1. Precursor ion beam

A fast beam of ions is extracted from a dc discharge, focused, and directed through a Wien velocity filter (crossed electric and magnetic fields). A Colutron model 100 ion source<sup>23</sup> is used to generate the ion beam. The source consists of a low-pressure gas discharge sustained by electron emission from a tungsten filament, with a pinhole in the anode. The potential between filament and anode is in the range 50–150 V. The anode is maintained at a high positive potential (3 kV in this work) with respect to the rest of the apparatus. The Colutron source is designed so that ions extracted through the pinhole originate in a small volume near anode potential. The resulting beam has a small energy spread, estimated to be only a few eV.

### 2. Charge-transfer neutralization

Once the appropriately mass-selected rare-gas-ion beam has been obtained at the desired beam velocity, approximately 0.1 to 1% of the ions are neutralized by symmetric charge transfer in a cell containing the same gas at approximately 0.1 mTorr. Residual ions are deflected to a current measuring plate. The cell has 0.64-cm-diameter entrance and exit apertures, 7.6 cm apart. Gas is admitted through a 0.64-cm tube; pressure is measured with a Baratron capacitance manometer connected through another 0.64 cm tube into the cell.

Symmetric charge transfer is a large-cross-section process, typically 10–30 Å<sup>2</sup> for the rare gases at several keV,<sup>24</sup> so the majority of collisions take place at large impact parameter and lead to very small angle scattering.

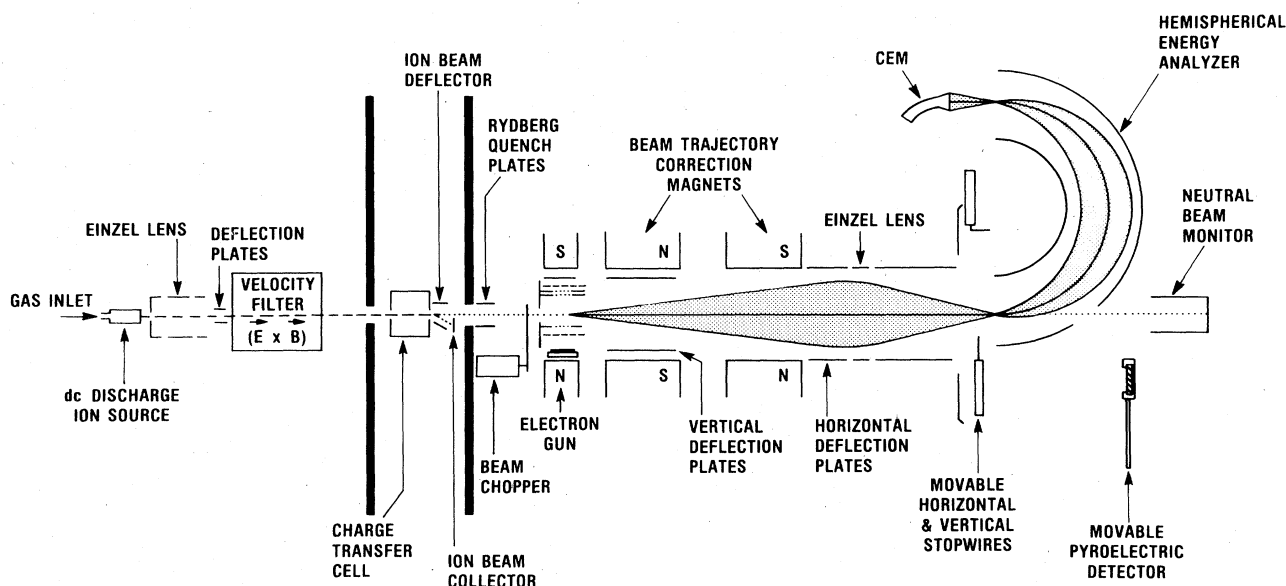


FIG. 1. Apparatus schematic.

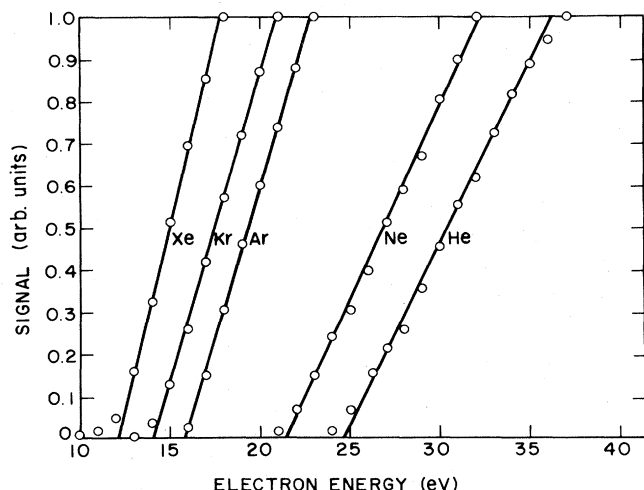


FIG. 2. Threshold region, from the data in Table IV, with straight line fits.

Thus, the resulting neutral beam remains collimated, and has the velocity of the incident ion beam. Fast neutral atoms scattered by more than about  $1^\circ$  are blocked by a 0.233-cm-square aperture in the ionization chamber.

The neutral beam is composed of nearly pure ground-state atoms, since all rare-gas excited states are far from energy resonance with the charge-transfer partner. Ionization threshold measurements (Fig. 2) show no evidence of metastable atoms. High Rydberg atoms with  $n$  above 19 are electric field ionized and removed by passing the beam between a pair of plates 5.1 cm long and 0.64 cm apart with 3 kV across them.

### 3. Neutral-beam flux measurement

The flux of the fast neutral beam is monitored by the secondary electron emission current  $I_{\text{sec}}$  from a metal surface located at, and electrically insulated from, the end of a Faraday cup, 3.2 cm diameter and 12.7 cm deep. We found that Nichrome V (80 at. % Cr, 20 at. % Ni) provides a stable secondary yield  $\gamma$  over a period of several hours, provided it is maintained at a temperature of about  $150^\circ\text{C}$  by radiation from a small quartz lamp mounted directly behind it (Fig. 3). All, or a constant fraction of the electrons from the Nichrome detector surface must be

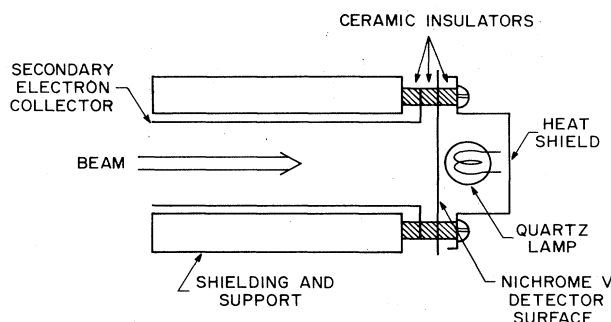


FIG. 3. Neutral-beam detector and Faraday cup.

collected and measured. Variation of the potential difference between the collector cylinder and the Nichrome surface shows that the current maximizes with the collector biased at +9 V. We believe this represents close to 100% collection, although a few percent of the electrons may be lost out the entrance of the tube.

Absolute measurement of the secondary yield  $\gamma$  is made with the help of a pyroelectric detector<sup>25</sup> (Fig. 4). The pyroelectric material<sup>26</sup> is lead zirconate titanate (PZT), 0.13 cm thick and 3.8 cm diameter, with silver electrodes on each face. The spontaneous polarization of the ceramic maintains a potential difference between the two electrodes. When a 3-keV beam strikes the PZT surface, the deposited power heats it slightly, and the expansion changes the voltage between the electrodes. The heat is conducted away with a time constant on the order of 1 sec. It is necessary to modulate the beam at a low frequency ( $\sim 1.5$  Hz was found to be a good compromise between response time and noise) and measure the modulated voltage with a lock-in detector. The sensitivity of our PZT is approximately  $1 \mu\text{V}/\mu\text{W}$ .

### 4. Neutral-beam shape

The shape of the neutral beam is measured at two locations within the instrument. To measure the shape near the neutral-beam—electron-beam collision region, a knife edge is scanned across the beam just in front of the 0.233 cm collimating aperture. The derivative of the detected signal gives the beam shape (Fig. 5). This measurement is made under computer control as part of each absolute ionization cross-section measurement.

Near the entrance to the hemispherical energy analyzer, the neutral-beam shape is measured via two movable stopwires which attenuate the transmitted beam. The vertical stopwire, 0.30 cm wide, positioned 53.3 cm beyond the 0.233 cm collimating aperture and 10.2 cm before the entrance to the Faraday cup, scans the beam in the horizontal direction. The horizontal stopwire, 0.15

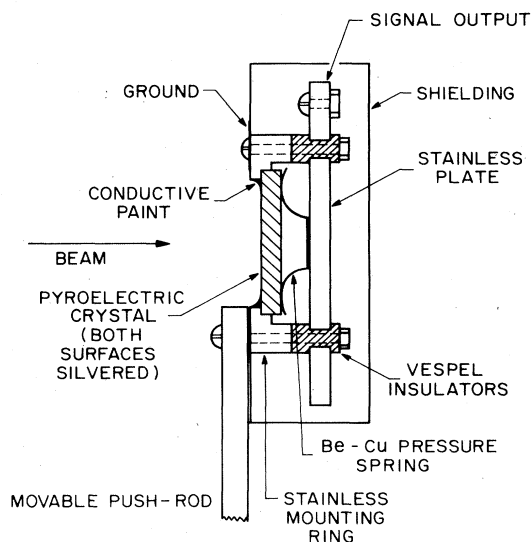


FIG. 4. Pyroelectric detector.

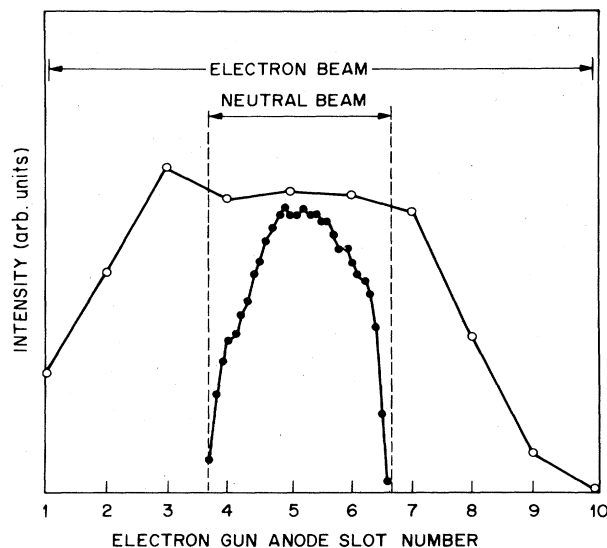


FIG. 5. Neutral- and electron-beam profiles at the collision region. Arrows show widths of the beam-defining apertures.

cm wide, is positioned approximately 1 cm closer to the Faraday cup. Figure 6 shows that the neutral beam is narrower than 1.2 cm at the baseline, near the entrance to the hemispheres. Thus, there is some divergence of the beam in the approximately 54 cm between the interaction region and the stopwires.

For an absolute measurement of the neutral-beam flux, all or a known fraction of the neutrals must strike the Ni-chrome detector surface. The size of the neutral beam is substantially smaller than the detector diameter (Fig. 6). Its centering on the detector is checked periodically with the stopwires. A small correction  $T$  is necessary to account for the transmission of the grid wires covering the hole in the hemispherical analyzer (Sec. III E); measurements of ion beam currents transmitted through this hole versus the current collected on the wires give a transmis-

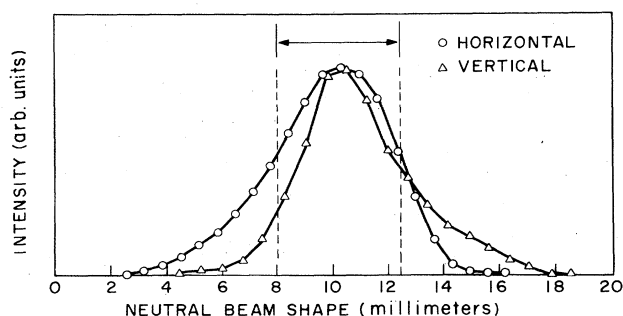


FIG. 6. Neutral-beam profiles at the stopwires. Stopwire widths have not been deconvoluted, so the true beam widths are slightly narrower. Collimating aperture width is indicated by the dotted lines.

sion of  $0.95 \pm 0.02$ .

Thus, the neutral-beam flux is given by

$$R = I_{\text{sec}}(1.602 \times 10^{-19} \gamma T). \quad (3)$$

## B. The electron beam

In its idealized form the electron beam would be uniform and exactly the same width as the neutral beam. A more practical design is to make one beam uniform and pass the other completely through the first. In this case the overlap factor  $F$  [Eq. (2)] reduces to a constant. We chose an electron gun design (Fig. 7) which to a rough approximation gives a uniform electron beam and has the built-in capability of continuously monitoring the profile.

### 1. Electrodes and potentials

The electron emitter is a planar cathode, 0.75 cm wide  $\times$  1.3 cm long, comprised of a barium-strontium oxide mixture on an indirectly heated nickel substrate.<sup>27</sup> The extraction grid (Fig. 7) is a planar photoetched tungsten grid of 81% transparency, made of 0.0051-cm wires on 0.051-cm centers. It is rigidly held about 0.064 cm from the cathode within an electron-beam defining aperture 0.47 cm wide and 0.74 cm long. The extraction grid is normally adjusted to about 6 V positive of the cathode, so that the current to the anode is 200–400  $\mu$ A.

The collision region where the electron beam crosses the neutral beam is defined by a pair of grids, held at nearly the same potential (actually 3.2 V apart to prevent trapping of thermal ions as discussed in Sec. II E 2). Both are constructed of parallel lengths of 0.04 mm tungsten wire spanning the width of the aperture. The bottom grid has a transparency of 95%, and the top grid has a transparency of 97%. The potential difference between the cathode and the bottom grid ( $A$  in Fig. 7) determines the energy of the ionizing electrons, and is established by a digital-to-analog converter under computer control.

After passing through the collision region, the electron beam crosses a 97% transparent suppressor grid (constructed of parallel tungsten wires) and is collected at an anode which is held at +70 V with respect to the collision region. The suppressor is at +9 V with respect to the collision region (and therefore –61 V with respect to the anode) so secondary electrons which leave the anode with less than 61 eV cannot return to the collision region.

The effects of spiraling by the electrons in a magnetic field (250 G here) have received much attention by previous workers.<sup>12,28,29</sup> Spiraling increases the effective path length, so if it occurs to any appreciable degree, it must be accounted for in calculating the overlap factor. It originates from any transverse velocity component the electron may acquire; sources are the thermal energy of electrons emitted from the cathode, deflection by inhomogeneous fields near the grid wires, and scattering off gas atoms or molecules. In this work, the gas pressure is so low ( $10^{-7}$  Torr) that only a negligible fraction of the electrons gain transverse velocity by scattering. The other

contributions are also negligible: The transverse component of the initial energy at the cathode, taken as  $kT$ , contributes less than a 0.1% increase to the path length at 100 eV and less than 1% at 10 eV. Deflection by fields near the grid wires contributes under 1%, estimated by Eq. (10) of Ref. 28. Overall, spiraling appears to have a negligible effect on the cross sections, consistent with the conclusion of Taylor *et al.*<sup>28</sup> for their electron gun with a similar magnetic field.

## 2. Anode designs

The anode has been designed to allow continuous sampling of the electron-beam shape in the direction transverse to the neutral beam. It consists of a planar molybdenum plate with ten slots, each 0.015 cm wide, centered 0.076 cm apart, and followed by ten corresponding gold collector strips on an alumina substrate. An analog-to-digital converter samples the current to those ten collectors periodically, with typical results as in Fig. 5.

A second anode was subsequently designed to reduce electron reflection (see Sec. II B 4). It does not, however, allow measurement of the electron-beam shape. It is constructed of five molybdenum plates, each 0.56 cm wide by 2.5 cm long, oriented so that the electron beam strikes at an angle of  $60^\circ$  with respect to the surface normal. The plates are positioned at 0.25 cm intervals and are surrounded on three sides by Mo back and side plates. The leading edges of the plates are chamfered, and the entire anode is coated with Aerodag G, a sprayable graphite, to further reduce electron reflection (by virtue of the low reflection coefficient of carbon; see below).

## 3. Electron-beam energy and energy spread

The energy spread of the electron beam has been estimated by examining the threshold region of the Xe cross-section curve. Since there was no apparent fine structure, the shape was modeled as the intersection of two straight lines, one being the background level and the other being an extrapolation of the straight line portion of the cross section curve a few eV above the ionization potential. The difference between these lines and the experimentally obtained shape approximates the energy spread. This procedure yielded an energy spread [full width at half maximum (FWHM)] of 0.7 eV, caused by the thermal energy spread due to the hot cathode, and by potential variations in the collision region from space charge<sup>30</sup> and the nonzero field across the collision region.

The average electron energy in the collision region differs from the applied voltage for several reasons: the contact potential difference between the cathode surface and the tungsten grids, space-charge depression of the potential, and the small electric field applied between the two collision region grids. This difference is measured by least-squares fitting the measured cross sections and adjusting the energy scales so that the  $x$  axis intercept agrees with the spectroscopic ionization potential. Although this procedure accurately compensates for the effect of space charge at threshold, a model<sup>30</sup> shows that the magnitude of the space-charge depression is a function of electron current and energy,  $\Delta V_{SC} \propto iE^{-1/2}$ . Thus at the currents we normally use  $\Delta V_{SC}$  should decrease nonlinearly from about 1.3 V at 12 eV to about 0.7 V to 200 eV. Given the absence of sharp structure in the rare-gas ionization cross

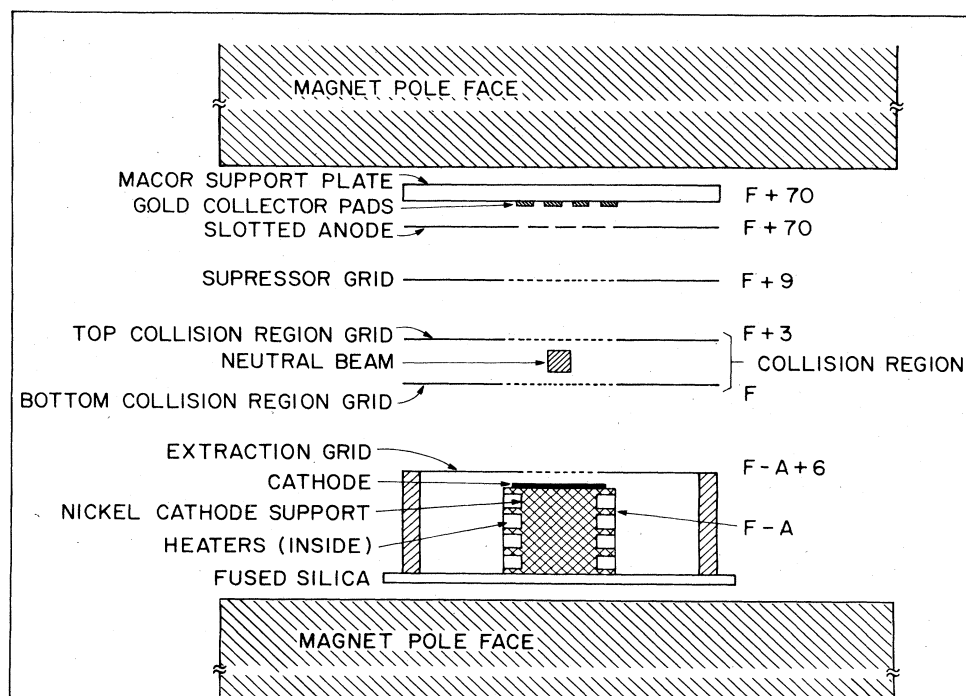


FIG. 7. Electron gun and voltages.  $F$  represents the collision region float voltage and  $A$  represents the electron-beam acceleration voltage.

sections, and the difficulty of calibrating the electron energy at energies above threshold, we neglect this effect.

#### 4. Secondary and reflected electrons

Secondary electrons and reflected primary electrons can perturb the cross-section measurement in two ways: through incorrect values of the electron current measurements, and by excess ionization of the neutral beam. We distinguish "true" secondary electrons with energy below 50 eV from elastically and inelastically reflected primary electrons with energies above 50 eV.<sup>31</sup> Since the secondary electron yields for both the tungsten grids and the Mo anode are roughly unity in the energy range of interest,<sup>32</sup> the effects deserve consideration.

We have examined secondary electron ejection within the gun by biasing the grids and anode to favor or suppress secondary ejection from each element, measuring the current to each element and comparing these data with those obtained when all elements are biased in their normal manner. The effect of secondary electron ejection from the extraction grid should be negligible, because the primaries strike it with only about 6 eV, and the very few secondaries which might form would have energies differing by less than 6 eV from the primaries. Secondary ejection from the bottom grid, however, affects the total current measurement because most of these secondaries are repelled by the cathode and are collected at the anode and upper grids. (The collimating magnetic field prevents losses out the sides of the gun.) Our measurements indicate that in the worst case, the total current may be overestimated by 3%. Secondary electrons from the top grid, suppressor grid, and anode perturb the total current measurement only if they are not ultimately collected by these elements. All of the secondaries from the anode are suppressed by the 70 V difference between the collision region and the anode. Secondaries ejected from the top and suppressor grids will either be immediately collected at the anode or they will traverse the collision region. Most of the latter will be repelled by the cathode field and will return to the anode except for a small fraction, perhaps 10%, which will be intercepted by the bottom grid. It is only those electrons collected at the bottom grid which perturb the total current measurement. Our analysis of the gun indicates that in the worst case (in which we assume all secondaries ejected from the top and suppressor grids reach the collision region) this current is 0.3% of the total measured current.

Ionization by secondary electrons is important only for those secondary electrons which traverse the collision region with an energy greater than the ionization potential of the species of interest. However, secondary electron distributions from metals typically peak below 8 eV,<sup>32</sup> with only a small component which extends to energies greater than the ionization potential. Thus, ionization by secondaries from the top and bottom collision region grids is caused by a small fraction of the secondaries, which in turn result from a current which is a small fraction of the primary current. The net effect should be negligible. Although there is undoubtedly an energy dependence to secondary electron yields and their effects, this aspect is

difficult to accurately model, and we have instead treated this by quoting worst-case uncertainties. The maximum error in the measured cross sections arising from the effects of secondary electrons is judged to be  $\pm 3\%$ .

The effects of electron reflection from the anode have been examined both experimentally and by modeling the process. In the model, we assume that all reflected electrons have energies within a few eV of the primary energy, an assumption which is probably correct for over 90% of the electrons. The main source of reflected electrons is the molybdenum anode because most of the primaries strike there. Reflected electrons travel back through the collision region, but if they have lost even a fraction of an eV due to inelastic processes they cannot return to the cathode. Thus, they pass once more through the collision region. On each of these passes, only a small percentage is intercepted by the grids. When a particular electron is collected and measured, it may have passed through the neutral beam three times. The net effect for the transparencies of our grids is that the effective electron current is  $(1 + 1.60\eta)$  times the measured electron current, where  $\eta$  is the coefficient of reflection from the anode. For polycrystalline molybdenum  $\eta$  is given in the literature as  $0.14 \pm 0.025$  for 160 eV electrons at normal incidence.<sup>33</sup> (This energy corresponds to 90 eV electrons in the collision region, approximately the energy at which our absolute cross-section measurements are made.) This model thus predicts the effective electron current to be 1.224 times the measured current for the planar Mo anode. If we assign a 20% uncertainty to our 1.60 geometry factor, the uncertainty in the 1.224 correction for reflected electrons is  $\pm 0.06$  or  $\pm 5\%$ .

A test of this reflection correction is to use the angled anode (Sec. IIB 2) to measure the rare-gas cross sections. We find that to obtain the same cross sections with the angled anode, the electron reflection correction must be reduced from 1.224 to 1.057. How reasonable is this value of 1.057? This anode reduces reflection both by trapping the reflected electrons and by the graphite surface coating, which has a literature reflection coefficient for normal incidence of only 0.08 near 160 eV.<sup>33,34</sup> For incidence at  $60^\circ$  with respect to the surface normal,  $\eta$  increases to 0.27.<sup>34</sup> If electrons reflect with a cosine distribution, approximately 60% of them strike an adjacent anode surface; only about 40% would escape. Furthermore, it is likely that electrons reflected from an angled surface reflect preferentially in the specular direction. This would further reduce the percentage of reflected electrons which escape from the anode. No data are available to determine this factor, but if we select an intuitively reasonable factor of 3 reduction in escaping electrons  $(1 + 1.60 \times 0.27 \times 0.40 \times 0.33)$ , the calculation can be made to match the observed reflection correction of 1.057.

#### 5. Expression for electron currents

The electron current through the collision region is taken as

$$I_e = (I_{TG} + I_S + I_A + I_C)(1 + 1.60\eta) \equiv I_e^m(1 + 1.60\eta), \quad (4)$$

i.e., the sum of the measured currents to the top grid of

the collision region, the suppressor grid, the anode, and the ten gold collector pads with a correction for the additional current due to reflected electrons. Typically, 2% of this sum comes from the top collision region grid, 2% from the suppressor grid, 85% from the anode, and 11% from the gold collectors. These currents are measured by analog-to-digital converters (ADC's) which are routinely calibrated with Keithley 160 and 177 multimeters to an accuracy of better than 0.5%.  $I_C$  is accurate to only  $\pm 2\%$ , because it is the sum of ten different measurements. Since  $I_e^m$  is determined primarily by  $I_A$ , we estimate its uncertainty to be less than 1%.

### C. Product ion collection

An accurate cross-section measurement requires either 100% collection or collection of a known fraction of ions formed in the collision region. The fast beam method used here makes it relatively easy to obtain 100% collection. Ions formed from the collimated neutral atom beam have 3 keV of translational energy in the forward direction, so they are barely deflected by momentum transfer from electron impact or by the weak electric fields in the collision region. Thus inertia carries the product ions out of the collision region and toward the detector.

#### 1. Beam steering and focusing

A complication is introduced by the magnetic field used to collimate the electron beam. Once an ion forms, it experiences a velocity-dependent transverse magnetic deflecting force. Ions therefore leave the collision region slightly off-axis and traveling at an angle to the axis. Although two pairs of electrostatic deflecting plates could redirect the beam along the axis, their settings would have to be changed for each ion species and each velocity. Our solution uses two additional magnets after the electron-beam collimating magnet (Fig. 1). The middle magnet redirects the beam toward the axis and the last one bends it back parallel to the axis. The electron-beam collimating magnet has  $3.2 \times 7.0$  cm poles (where the dimension along the beam is given first), a 4.9 cm gap, and a 250 G field (although ions experience this field only from the approximate midpoint of the magnet where they are formed). The middle magnet has  $6.4 \times 7.0$  cm poles, a 4.0 cm gap, and a 160 G field (oriented antiparallel to the fields in the other two), and the last has  $6.4 \times 7.0$  cm poles at 4.9 cm gap, and a 60 G field. The accuracy with which this magnet triplet reflects the beam is limited by magnetic field fringing and inhomogeneity. Fields were adjusted by trial and error, either by remagnetizing one or more of the magnets, or by varying the gap. Stopwires (Fig. 1) were used to determine the position of the ion beam with respect to the neutral beam. The net effect of this magnet triplet is to direct ions close to the axis, regardless of the species or velocity.

The final direction adjustments are made with electrostatic deflection plates. Vertical deflection is effected by plates mounted between the poles of the middle magnet, and horizontal deflection by the two halves of the first

cylinder of the einzel lens (see below), which has been split.

Although the ion beam nearly follows the trajectory of the collimated neutral beam, neither remains perfectly collimated. We focus the ion beam by using a three-element electrostatic einzel lens consisting of three cylinders, 6.4 cm diameter, separated by 0.64 cm gaps, with the first and third elements grounded and the 3.2-cm-long middle element run at a positive voltage typically 80–90 % of the beam's translational energy. The overlap volume between the electron beam and the neutral beam in the collision region is taken as the object. It is located 35 cm before the midpoint of the lens. The desired image plane is at the entrance of the hemispherical analyzer (see below), located 19 cm beyond the midpoint of the lens. This should give an image about half the size of the object. With the center element of the einzel lens at 0.9 times the beam energy, the image is measured to be only a 0.20 cm spot, confirming that even with the apparatus imperfections, it can produce an image which is smaller than the object (the 0.233 cm neutral-beam defining aperture).

#### 2. Charge state and energy analysis

A concentric hemispherical energy analyzer is used to separate the ion beam from the neutral beam and to separate ions of different charge states. Although a uniform deflecting electric field might suffice for these experiments on atoms, this more complex device is necessary for experiments on dissociative ionization of molecules because the two-dimensional focusing permits complete collection of the fragment ions. This point will be expanded upon in a future publication.

The energy analyzer consists of two concentric stainless-steel hemispheres, of radii 6.50 and 10.24 cm, with no correction for fringing fields. The ion beam enters at a point midway between the spheres (at a radial position of 8.37 cm). For ions to be focused on the midpoint in the exit plane, the relationship between the voltages applied to the hemispheres and the initial energy of the transmitted ions is<sup>35</sup>

$$V_2 - V_1 = (R_2/R_1 - R_1/R_2) \times [E_0 - V_2 + R_1(V_2 - V_1)/(R_1 + R_2)], \quad (5)$$

where  $R_1$  and  $R_2$  are the radii of the inner and outer hemispheres, respectively,  $V_1$  and  $V_2$  are the applied voltages, and  $E_0$  is the translational energy of the ion before it enters the field of the analyzer. In the case of singly charged ions, all experiments reported here utilized  $E_0 = 3200$  eV (3000 eV neutral energy + 200 eV resulting from floating the collision region off ground, see Sec. II E 1). The voltages  $V_1$  and  $V_2$  typically employed are approximately  $-1840$  and  $+1200$  V, respectively.

#### 3. Ion collection

Ions which leave the hemispherical analyzer travel 3.8 cm and strike the 0.95-cm-diameter entrance cone of a Galileo model 4830 channel electron multiplier (CEM). The ion beam is directed to the center of the CEM by adjusting both the voltage applied to the vertical deflection

plates and that applied to the outer hemisphere. The ion beam may be scanned across the CEM face by ramping the outer hemisphere voltage; plots of the CEM output versus scan voltage for the rare-gas ions are shown in Fig. 8. The flat tops of these plots indicate that the transmitted ion-beam diameter is smaller than the entrance of the CEM.

All of these arguments show that 100% collection is obtained: There are no apertures smaller than the CEM entrance to intercept any ions. Deflection of the ions by electron space charge or momentum transfer is well controlled, as illustrated by the small focus at the entrance to the hemispheres. This image is again focused by the hemispheres to a spot small compared to the CEM entrance. Loss by collisions with the background gas at  $10^{-7}$  Torr is negligible. One-hundred percent ion collection is ex-

pressed in Eq. (8) by a transmission constant  $K$  with a value of unity.

#### D. Ion detection efficiency

The CEM is run at a high enough voltage (3.5 kV) to produce saturated output pulses which are then amplified, discriminated, and counted with a MINC 11/23 computer. Counting system deadtime is accounted for in the limit of low count rates by<sup>36</sup>

$$C_{\text{corr}} = C / (1 - C\tau), \quad (6)$$

where  $C$  is the measured count rate,  $C_{\text{corr}}$  is the corrected count, and  $\tau$  is the deadtime of  $2 \mu\text{sec}$ . For the maximum count rates used here, about  $10^4/\text{sec}$ , this correction is only about 2%.  $C$  is measured with a crystal time base, accurate to better than 0.01%.

Efficiency of the detector  $\epsilon$  must be known for accurate cross-section measurements, a point stressed in several recent publications.<sup>5,13,37</sup> In principle, it is possible to evaluate  $\epsilon$  by comparing the number of output pulses per second to the ion current measured with a Faraday cup and sensitive electrometer. Such a calibration, however, requires the accurate measurement of very low currents, and is not possible with our present apparatus. Therefore, we operate under conditions which maximize  $\epsilon$ , and assign an approximate value to it, with guidance from studies of similar CEM detectors.<sup>18,37-39</sup>

For convenience, we divide epsilon into three factors

$$\epsilon = \epsilon_1 \epsilon_2 \epsilon_3. \quad (7)$$

$\epsilon_1$  is the probability that an incident ion ejects at least one electron upon impact with the CEM. Obviously, an impact event which does not lead to secondary electron ejection will not be counted. Ions which produce multiple secondary electrons are counted as only one event because all the electrons lie well within the  $2 \mu\text{sec}$  deadtime of the detection system. Thus, the absolute upper limit of  $\epsilon_1$  is unity, corresponding to at least one secondary electron for every incident ion. The only possibility of a higher value would be if the CEM generated multiple pulses further apart than the dead time of the electronics, and no such multiple pulses appear when we view the CEM output with a fast oscilloscope.

Although we cannot set a lower limit to  $\epsilon_1$ , we expect it to be near unity. For sufficiently high impact energy, every ion should generate at least one secondary electron. In this work, the energy of singly charged ions upon CEM impact was no lower than 6200 eV (from the 3000 eV neutral-beam energy, the 200 V collision region float voltage, and at least -3000 V on the face of the CEM). We examined the effect of increased ion kinetic energy on the CEM signal count rate by floating the entire CEM between 0 and -1800 V. These experiments yielded no clear evidence of a detection efficiency increase of more than a few percent. This behavior is consistent with the results of most studies in the literature; detection efficiencies appear to reach their maximum values by 6000 V.<sup>37-39</sup> (In one careful study of  $\text{Ne}^+$ , however, with a Bendix 4700 CEM very similar to ours,<sup>18,40</sup> a plateau was not reached until 10 keV.) Multiply charged ions strike

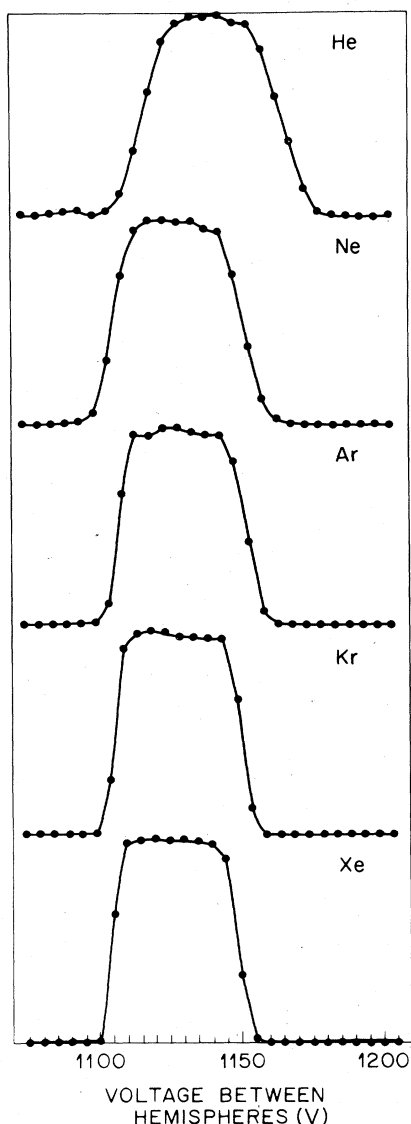


FIG. 8. Scans of the ion beams across the face of the CEM. The flat tops demonstrate collection of the entire beams.



the CEM with greater energy, due to their greater acceleration to the CEM (doubly and triply charged ions strike with at least 9400 and 12600 eV, respectively) and so must have detection efficiencies greater than or equal to those for singly charged ions. The close agreement between our ratios for multiple to single ionization (see below) and those of Stephan *et al.*<sup>20,22</sup> suggests that the efficiencies are nearly equal, and therefore near unity. Considering all these factors, we estimate  $\epsilon_1$  to be  $0.95 \pm 0.05$ .

$\epsilon_2$  is the probability that a secondary electron created at the CEM entrance cone is accelerated down the CEM channel without being lost to the surrounding apparatus. The design of the CEM causes this to happen with high efficiency, although for a sufficiently high negative voltage on the CEM cone, a decrease of several percent has been observed in the CEM output, as secondary electrons are drawn to nearby grounded surfaces. We estimate  $\epsilon_2$  to be  $0.95 \pm 0.05$ . An obvious future apparatus change is to prevent this loss by adding a negatively biased guard ring in front of the CEM.

$\epsilon_3$  is the probability that an electron reaching the CEM channel is amplified to a large enough output pulse to exceed the discriminator threshold. An indication that all pulses exceed the counting threshold is that the signal count saturates as the high voltage across the CEM is increased above 3000 V. Thus, we take  $\epsilon_3$  to be 1.0.

The resulting value of  $\epsilon$  is  $0.90 \pm 0.07$ , where the 0.07 uncertainty is nearly large enough to encompass both the upper limit of unity and the  $\epsilon$  value of 0.78 given by Ref. 18. In the absence of a direct measurement, we use  $\epsilon = 0.90$  for all our measurements.

When all of the factors related to ion counting efficiency are combined,  $I_i$  is given by

$$I_i = 1.602 \times 10^{-19} C_{\text{corr}} / K \epsilon_1 \epsilon_2 \epsilon_3, \quad (8)$$

where  $K = 1$  represents the fraction of ions transmitted to the CEM face.

### E. Background corrections

Background is defined as any counts other than those from the ionization process we are trying to measure. "Trivial" sources of background such as CEM dark counts, scattered electrons or photons from the electron gun, or defects in high-voltage wiring are negligible, as shown by a count rate of under one per second when a 70 eV electron beam is present and the ionization chamber is isolated from the preceding two chambers. Three sources of background have definitely been observed in this apparatus, however: collisional ionization, charge transfer with trapped ions, and Rydberg atoms in the fast beam.

#### 1. Collision ionization

The most serious source of background, collisional ionization, occurs when a fast neutral atom collides with a thermal neutral atom or molecule from the  $10^{-7}$  Torr residual gas. The collision might take place anywhere along the trajectory, from before the collision region to the entrance of the hemispheres, with the resulting ion being able to reach the CEM. A partial correction is to

modulate the electron beam on and off by applying a 1 Hz square wave to the extraction grid; the counts with the electron beam on are signal plus background, the counts with the electron beam off are background, and the difference of these two count rates is the signal. This procedure is equivalent to that of Harrison,<sup>4</sup> except that with effectively zero counts in the absence of the neutral beam, we do not require modulation of the neutral beam. Unfortunately, background subtraction cannot remove the shot noise from a large collisional ionization background. This problem can be ameliorated by electrically floating the collision region several hundred volts above ground<sup>41</sup> and adjusting the hemispherical energy analyzer to pass ions with the sum of the neutral-beam kinetic energy and the float voltage. Many of the ions from collisional ionization have several hundred eV less energy and are deflected away from the CEM. Only those background ions which are formed by collisional ionization within the collision region are still detected. The result of this procedure is illustrated in Fig. 9, where the background is the large peak and the signal is the smaller flat-topped peak on the right.

#### 2. Charge transfer with trapped ions

Another source of background is ionization of a fast neutral atom by charge transfer with a thermal ion trapped in the space charge of the electron beam.<sup>41</sup> Although such collisions are infrequent, only one beam atom in about  $10^7$  must be ionized to produce background comparable to the signal from electron-impact ionization. This could be produced by a reasonable trapped ion density of  $10^7 \text{ cm}^{-3}$ , a neutral-beam flux of  $10^{10}/\text{sec}$ , and a charge-transfer cross section of  $2 \times 10^{-16} \text{ cm}^2$ . Two solutions to this problem were found. One is to reduce the gas flow into the ionization chamber by reducing the pressure in the charge-transfer chamber, so there is less residual gas to be ionized in the electron gun. The other is to apply a small electric field (6.4 V/cm) across the collision region to extract the trapped ions and thermalized electrons. This is accomplished with a 3.2 V battery across the collision region plates which are 0.5 cm apart. The resulting potential variation of 1.6 V across the 0.233-cm-

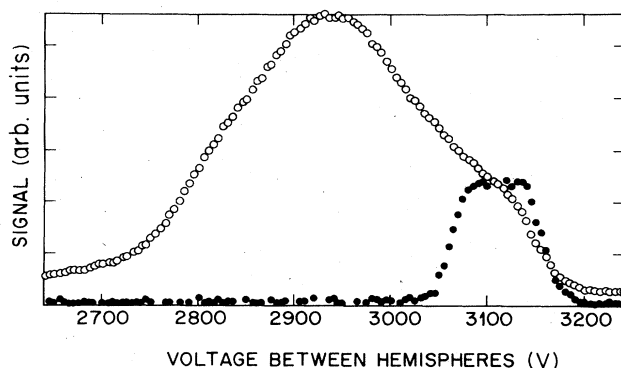


FIG. 9. Scans of an  $\text{Ar}^+$  beam across the face of the CEM, showing that floating the collision region shifts the signal (solid circles) away from the most intense background (open circles).

high neutral beam degrades resolution slightly, but this is unimportant except at threshold.

### 3. Rydberg atoms

Rydberg atoms with principal quantum number  $n$  between approximately 8 and 19 can be present in the neutral beam as it passes through the electron beam. Those with  $n$  above 19 are removed by electric field ionization in the Rydberg quench region (Fig. 1).<sup>42</sup> Those with  $n$  less than approximately 8 have radiative lifetimes shorter than their transit times from the charge transfer cell to the electron gun.<sup>42</sup> Those with  $8 < n < 19$  remain in the beam and are a potential source of error in the ground-state cross-section measurements. The size of the contribution from ionization of Rydbergs at 100 eV is given by

$$c^{100}(8 < n < 19) = c_{3000}^{100} \frac{c_{200}^{100} - c_{3000}^{100}}{c_{200}^{10} - c_{3000}^{10}}, \quad (9)$$

where  $c$  is the ion count rate, the superscript is the electron energy in eV, and the subscript is the voltage across the Rydberg quench plates. This procedure measures for  $8 < n < 37$  the ratio of the Rydberg ionization cross section at 100 eV ( $c_{200}^{100} - c_{3000}^{100}$ ) to that of 10 eV ( $c_{200}^{10} - c_{3000}^{10}$ ). Because a large range of  $n$ 's is included, the signal is large enough to measure with some accuracy. Multiplication of the Rydberg signal at 10 eV for  $8 < n < 19$  by this ratio then gives the number we want. This analysis was applied to many of the measurements, but produced only statistically insignificant corrections to the absolute cross section (no larger than 1 or 2%). The results reported here, therefore, do not include any correction for Rydberg atoms.

## III. ABSOLUTE CROSS-SECTION MEASUREMENT PROCEDURES

An absolute cross-section measurement consists of measuring each of the factors in Eqs. (1) and (2) at a single electron energy. We describe these measurements in terms of the directly measured quantities, and combine them at the end of the section to obtain the working expression for the cross section. The sequence of measurements is important, to minimize drifts and to prevent the measurements themselves from causing any unwanted apparatus changes.

It is well known that absolute cross-section measurements are subject to a multitude of experimental errors. Thus, a careful analysis and assessment of the sources of error is necessary. Many points have been discussed already. In Table I we list each of the primary measured quantities and its assigned systematic uncertainty.

### A. The overlap factor

The electron-beam—neutral-beam overlap factor is measured first. The neutral-beam profile is obtained by scanning a knife edge across the neutral-beam aperture and taking the derivative of the transmitted neutral flux versus position data. The width of the neutral beam is defined by the  $0.233 \pm 0.002$ -cm-wide collimating aperture;

TABLE I. Estimated systematic uncertainties for each of the measured quantities in Eq. (14).

Quantity in Eq. (1)	Typical value	Quantity in Eq. (14)	% uncertainty
$R$	$10^{10}/\text{sec}$	$I_{\text{sec}}$	2
		$T$	2
		$\gamma$	3
$I_e$	$300 \mu\text{A}$	$I_e^m = I_{\text{TG}} + I_S + I_A + I_C$	1
		$\eta$	5
		Secondary	3
$F$	$2.0 \text{ cm}^{-1}$	Electron-beam profile	5
$v_n$	$10^7 \text{ cm/sec}$	$v_n$	< 1
		$v_e$	< 1
$I_i$	$10^{-16} \text{ A}$	$C_{\text{corr}}$	0
		$K$	0
		$\epsilon_1 \epsilon_2 \epsilon_3$	8
Total (in quadrature)			12

this gives the full-scale width of the neutral-beam profile (Fig. 5). The electron beam is measured at ten discrete positions, using the gold collector pads behind the slotted anode. Thus Eq. (2) is approximated by

$$F = \frac{I_4 N_4 + I_5 N_5 + I_6 N_6}{\sum_i I_i (N_4 + N_5 + N_6) 0.33 W}, \quad (10)$$

where  $\sum_i I_i$  is the sum of the currents to the 10 collector pads,  $I_4$  is the electron current to pad 4, etc.,  $N_4$  is the relative intensity of the neutral beam in a slice of width 0.076 cm centered at pad 4, etc., and  $W$  is the  $0.233 \pm 0.002$  cm width of the neutral beam. The overlap factors measured over several months varied very little, from 1.9 to  $2.1 \text{ cm}^{-1}$ . The value of  $F$  differs so much from unity primarily because the electron beam is much wider than the neutral beam.

For this measurement of  $F$  to be valid, it is necessary as Kieffer and Dunn<sup>12</sup> point out that neither beam diverges over the region of intersection. The neutral beam easily satisfies this requirement; Figs. 5 and 6 show that it diverges only about 0.6 cm in the 54 cm between the aperture and the stopwire. The possibility exists, however, for spreading of the electron beam between the aperture and the slotted anode, since we measure a change in the strength of the collimating magnetic field across this region. Calculations indicate that this spreading of the electron beam could lead to errors in the electron beam profile of no more than  $\pm 5\%$ . A small degree of spreading is indicated by the width of the electron beam at the slotted anode (Fig. 5), but this measured spreading is smaller than 5%. There exists also the potential for a small error in  $\sum_i I_i$  (the sum of the electron currents at each of the collector pads) since the electron-beam current does not fall to zero at pad 1. We believe the combined errors in the electron beam profile do not exceed  $\pm 5\%$ .

A necessary test of the overlap calculation is that the calculated cross section be independent of the overlap factor. This was examined by varying the neutral-beam shape and plotting  $C_{\text{corr}}/(I_{\text{sec}} I_e^m F)$  versus  $F$ . (The

neutral-beam shape was varied by changing the shape of the ion beam with the Wien filter.) The range of overlap factors examined was much wider than those normally obtained during cross-section measurements, and included many which would be rejected under normal operating conditions due to the inhomogeneity of the beam. The data indicate that the calculated cross section varies less than 1% over the wide range of overlap factors examined. Thus, we conclude that the overlap factor effectively compensates for beam inhomogeneities in the cross-section determination.

### B. The normalized signal

Next the normalized ion signal is measured at the same electron energy, with the electron current alternately on and off for 0.5 sec. The normalized signal is defined by

$$I_{\text{norm}} = C_{\text{corr}} / I_{\text{sec}} I_e^m, \quad (11)$$

a quantity which contains the variable factors of  $I_i / I_e R$ . The difference count  $C_{\text{corr}}$  is stored as the signal. Data acquisition times vary between 1 and 10 min, depending upon the signal-noise ratio.  $F$  and  $I_{\text{norm}}$  are then remeasured to verify the absence of drifts.

### C. The secondary yield $\gamma$

Finally, the secondary emission coefficient  $\gamma$  of the Nichrome surface is measured. The procedure uses a pyroelectric detector to relate the secondary electron current from the unknown neutral beam to the measured current of a reference ion beam. Both the unknown neutral beam and the reference ion beam are modulated at the same frequency by a knife-edge chopper just in front of the neutral-beam defining aperture.  $\gamma$  is given by

$$\gamma = V_+ I_{\text{sec}}(\text{mod}) / V_0 I_+(\text{mod}), \quad (12)$$

where  $V_+$  and  $V_0$  are the responses of a lock-in detector to the output of the pyroelectric detector for the reference ion beam and the unknown neutral beam, respectively,  $I_{\text{sec}}(\text{mod})$  is the averaged secondary electron current measured when the modulated neutral beam strikes the Nichrome surface, and  $I_+(\text{mod})$  is the averaged current of the modulated ion beam, measured by the Faraday cup.

The sequence of measurements is important, because some steps of the measurement process have been found to alter the value of  $\gamma$ , presumably by damaging the Nichrome surface. Thus, the relatively weak modulated neutral beam is measured first, followed by measurement of the more intense ion beam. To begin, the pyroelectric detector is placed in the path of the chopped neutral beam and  $V_0$  is measured; a 30 sec average is taken of readings sampled by an analog-to-digital converter at a 60 Hz rate. The pyroelectric detector is then withdrawn so that  $I_{\text{sec}}(\text{mod})$  can be measured. Next, an ion beam of the same species, energy, and modulation frequency is directed through the apparatus and centered on the Nichrome surface. The pyroelectric detector is moved back to intercept this ion beam, and  $V_+$  is measured in the same way that  $V_0$  was measured. Finally, the pyroelectric detector is withdrawn and  $I_+(\text{mod})$  is measured with the neutral-

beam detector, reconfigured as a Faraday cup.

Several effects contribute to the systematic uncertainty of  $\gamma$ . (1) Drift in the sensitivity of the Nichrome surface is usually less than 1% over a period of 10 min. Since the time between the measurement of  $\gamma$  and the normalized signal is only 1 min, this error should be negligible. (2) A key assumption is that the pyroelectric response to the ion beam is the same as it is to a neutral beam of the same species and with the same energy. Since the ion and neutral beams have the same mean kinetic energy (3 keV) and nearly identical kinetic energy distributions, the only relevant difference between them is the potential energy of the ion (which ranges from 12.1 to 25.6 eV). Although neutralization of the ion at the pyroelectric surface is expected to lead to slightly enhanced secondary electron emission over neutral impact, the difference in the energy brought to the surface by this process is negligible. Similarly, although the energy carried away from the pyroelectric ceramic by sputtered particles could be as much as 5% of the incident energy, the difference for the incident ions and neutrals of the same mass and energy should be well under 1%. (3) The efficiency of the pyroelectric detector is found to vary by less than 7% as it is scanned across the central 3 cm. Thus we focus the ion beam to approximately the same size as the neutral beam and deflect it to the same position. The residual error is taken as  $\pm 2\%$ . (4) Any absolute errors in the calibration of the lock-in amplifier and ADC's cancel, since the same devices are used to measure  $V_+ / V_0$ , and  $I_{\text{sec}}(\text{mod}) / I_+(\text{mod})$ . The overall systematic uncertainty in  $\gamma$  is therefore  $\pm 3\%$ .

### D. The beam velocities

The velocity factors  $v_n$  and  $v_e$  are known with high accuracy.  $v_n$  is determined by the potential difference between the point near the Coultron anode where the ion forms (expected to be within several volts of the anode potential<sup>21</sup>), and the charge-transfer chamber which is at ground potential. Thus, a conservative estimate of the potential difference is  $3000 \pm 50$  V, so

$$v_n (\text{cm/s}) = 1.389 \times 10^6 [(3000 \pm 50) / M]^{1/2} \quad (13)$$

with an uncertainty of under 1% (where  $M$  is the atomic mass). The energy transfer accompanying charge transfer should also be negligible, since only forward scattered neutrals pass through the aperture.  $v_e$  is given by the potential difference between the cathode and the collision region, with a maximum uncertainty of  $\sim 5\%$  near threshold and decreasing at higher electron energy. This is totally negligible, however, because in the limit that  $v_e \gg v_n$ ,  $v_e$  drops out of Eq. (1). The maximum error in this approximation is 0.7% for the lightest atom, helium, and at electron energies near threshold. Overall, the uncertainty in  $v_n$  is under 1%.

### E. The working expression for the cross section

Combining Eqs. (1), (3), (4), (8), and (13), we get for the absolute cross section at the fixed electron energy of the measurement (valid for a 3.0 keV beam):

$$\sigma(\text{cm}^2) = \frac{1.952 \times 10^{-30} C_{\text{corr}} \gamma T}{I_{\text{sec}} K \epsilon F M^{1/2} I_e^m (1 + 1.60\eta)} \quad (14)$$

When all the uncertainties (Table I) are added in quadrature, we obtain what we believe is a realistic estimate of the overall systematic uncertainties of these absolute cross sections:  $\pm 12\%$ .

#### IV. RESULTS AND DISCUSSION

Three kinds of measurements are made. An absolute cross-section determination is typically made at a single electron energy near the cross-section maximum for single ionization. The energy dependence of the cross section and multiple to single ion ratios, both relative measurements, are then made and scaled to an absolute cross section.

##### A. Absolute cross sections

Absolute single-ionization cross sections were measured for each rare gas. The individual measurements, their means and their random errors (one standard deviation) are shown in Fig. 10. The random errors range from 5% for Xe to 11% for Ar. The overall uncertainties (one standard deviation) are obtained by combining these random errors in quadrature with our calculated systematic error of  $\pm 12\%$ , and are included in Fig. 10.

Ratios of cross sections for double to single ionization were measured for Ar, Kr, and Xe at 100 eV. Triple- to single-ionization ratios were measured for Kr and Xe at 150 eV. These values are given in Table II and are included in Fig. 11 as the most recent point (1986), along with ratios measured by previous workers.<sup>20,21,43-53</sup> In most

TABLE II. Measured ratios of cross section for multiple to single ionization.

	Electron Energy (eV)	This work	Stephan <i>et al.</i> <sup>a,b</sup>
$100\sigma(\text{Ar}^{2+})$	100	$6.51 \pm 0.13$	$6.8 \pm 0.2^a$
$\sigma(\text{Ar}^+)$			
$100\sigma(\text{Kr}^{2+})$	100	$8.60 \pm 0.09$	$8.7 \pm 0.3^a$
$\sigma(\text{Kr}^+)$			
$100\sigma(\text{Kr}^{3+})$	150	$0.70 \pm 0.01$	$0.65 \pm 0.04^a$
$\sigma(\text{Kr}^+)$			
$100\sigma(\text{Xe}^{2+})$	100	$10.50 \pm 0.35$	$10.8^b$
$\sigma(\text{Xe}^+)$			
$100\sigma(\text{Xe}^{3+})$	150	$4.28 \pm 0.19$	$4.1^b$
$\sigma(\text{Xe}^+)$			

<sup>a</sup>Reference 20.

<sup>b</sup>Reference 22.

cases, the disagreement is large, with the exception of  $\sigma(\text{Ar}^{2+})/\sigma(\text{Ar}^+)$ , for which four of the most recent five measurements cluster near 0.07. These are the experiments which, as Stephen, Helm, and Märk<sup>20</sup> (SHM) have pointed out, paid greatest attention to eliminating systematic errors. All five of our measured ratios agree with those of SHM to within experimental error (Table II). This agreement lends confidence to the ratios reported by SHM for other multiply charged ions which we did not measure.

The uncertainties of these multiple-ionization ratios are dominated by the random measurement errors, from 1 to 4%. The systematic errors are much smaller than those

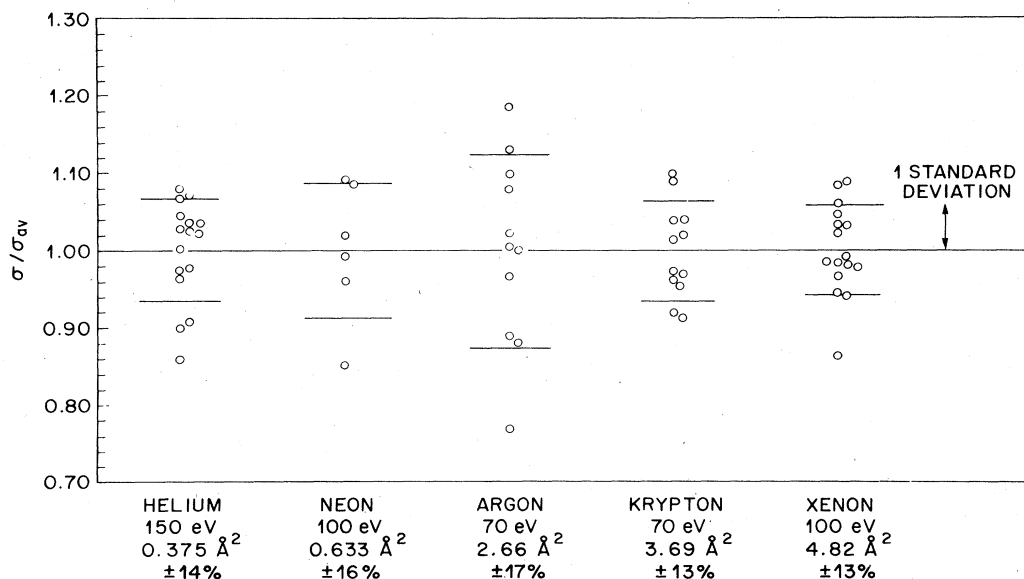


FIG. 10. Individual absolute cross-section measurements for single ionization. Average cross sections are given at the bottom of the figure, along with the combined (in quadrature) systematic and statistical uncertainties.

for single ionization because most sources of error are identical for the single and multiply charged ions. The major concern is that  $\epsilon_2$  may differ for ions of different charge and different energy, since the higher charged ions are accelerated more strongly to the CEM. The agreement with SHM's ratios argues that this effect is negligible, however; SHM used a Faraday cup to calibrate their multiplier, so there should be no charge-state discrimination in their measurements. Moreover, Nagy *et al.*<sup>16</sup> re-

port no efficiency difference for all five rare gases, and no difference for the detection efficiency of doubly and triply charged ions when their velocities equaled those of 10 keV singly charged ions.

We calculate absolute total cross sections according to  $\sigma_T = \sigma^+ + 2\sigma^{2+} + 3\sigma^{3+}$  and compare the results to previous work in Table III. For He, Ne, Ar, and Kr, the agreement among our data, REG,<sup>15</sup> Montague *et al.*,<sup>19</sup> and Kurepa *et al.*<sup>16</sup> is excellent, all values lying within each individual error estimate, and the quoted values all agreeing with each other to better than 6%. The Ne and Ar results of Fletcher and Cowling<sup>17</sup> lie slightly higher than the rest, but with overlapping error estimates. Disagreement with the results of Schram *et al.*<sup>54</sup> is more serious, particularly for He, although to make these comparisons at the energies of our measurements, we have been forced to interpolate or extrapolate those values in parentheses, so the comparisons are less reliable.

Xenon shows the major disagreement; our value lies 12% above that of REG, well above the upper limit of their quoted uncertainty, while their value is at the lower extreme of our uncertainty. Of the five gases, Xe is the easiest for us to measure because it gives the largest signal and the smallest background. Moreover, we know of no systematic error in our method which would be significantly greater for Xe than for any of the other four rare gases. The disagreement might originate with REG's pressure measurement. In their test of the validity of the assumption of free molecular flow (their Table IX),<sup>15</sup> xenon passed the test least satisfactorily. They also noted that their use of a McLeod gauge to measure Xe pressure gave a cross section 27% higher than the effusive flow method, and concluded that "Xe has a singularly large McLeod gauge error," far larger than the McLeod error for any other gas, including their 8% value for Kr and their 12% value of Ar. Schram *et al.*<sup>55</sup> attempted to measure McLeod gauge corrections and found only a 14% correction for Xe, compared to 10% for Kr and 8% for Ar. Although these corrections are not transferable between the two instruments, the 27% value is suspiciously high. An assumed 18% correction to REG's McLeod gauge measurement would give agreement with our xenon cross section. One last argument that REG's Xe cross section is suspiciously low is their comparison to the high energy data of Schram *et al.*,<sup>55</sup> that data is about 20% lower than REG's for He and Ne, about 8% lower for Ar and Kr, but 8% higher for Xe. These two data sets would be in much better agreement if the REG Xe cross section were raised to the value we measure. Although these arguments are not conclusive, they do support the larger Xe cross section.

### B. Thresholds

The threshold regions for single ionization are shown in Fig. 2. The threshold is taken as the x-axis intercept of the cross section as determined by linear least-squares fits of the data for about the first 10 eV above threshold, and the energy scale is adjusted to make this agree with the spectroscopic ionization potential. Fine structure is not observed in our data, because of signal-to-noise limitations

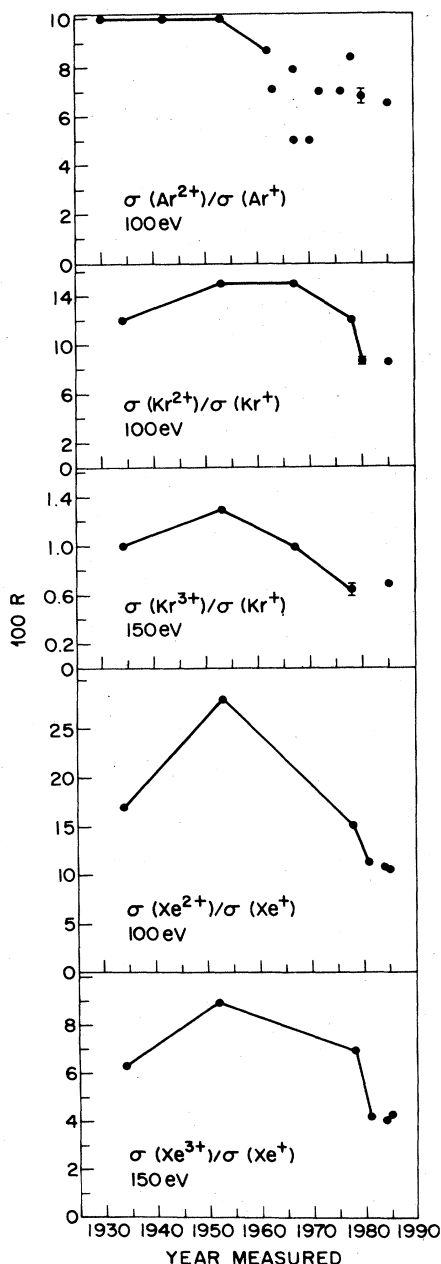


FIG. 11. Ratios for multiple to single ionization as measured over the past 50 years by Refs. 43–53, 20, and this work. ( $R$  represents the ratio here.)

TABLE III. Absolute total ionization cross sections ( $\text{\AA}^2$ ).

Energy (eV)	$\sigma_T$ ( $\text{\AA}^2$ )				
	He 150	Ne 100	Ar 70	Kr 70	Xe 100
This work	$0.377 \pm 0.053$	$0.645 \pm 0.098$	$2.93 \pm 0.49$	$4.19 \pm 0.57$	$6.03 \pm 0.80$
Rapp and Englander-Golden <sup>a</sup>	$0.368 \pm 0.026$	$0.667 \pm 0.047$	$2.77 \pm 0.19$	$4.21 \pm 0.29$	$5.38 \pm 0.38$
Montague <i>et al.</i> <sup>b</sup>	$0.364 \pm 0.017$				
Kurepa <i>et al.</i> <sup>c</sup>			$2.87 \pm 0.14$		
Fletcher and Cowling <sup>d</sup>		$0.695 \pm 0.028$	$3.01 \pm 0.12$		
Schram <i>et al.</i> <sup>e</sup>	(0.316)	0.639	(2.69)	(4.45)	6.21

<sup>a</sup>Reference 15.<sup>b</sup>Reference 19.<sup>c</sup>Reference 16.<sup>d</sup>Reference 17.<sup>e</sup>Reference 54.

and the 0.7 eV energy spread, so it is ignored in this analysis. The largest effect fine structure might have is for Xe, where our extrapolation could give an x-axis intercept about 0.35 eV about the ionization potential.<sup>56</sup> The values of Table IV include this energy scale calibration. As a check, the thresholds calculated from linear least squares fits of Table IV and given in Table V agree with spectroscopic ionization potentials<sup>57</sup> within 0.1 eV for all five rare gases. Similar extrapolations of the data of REG lie within 0.3 eV of the spectroscopic thresholds. Thresholds are difficult to calculate from the data of SHM be-

cause they report cross sections at 5 eV intervals; their extrapolated thresholds differ from spectroscopic by up to 0.66 eV.

The energy scale determined from single ionization is also used for multiple ionization. Plots of the threshold regions for double ionization were found to rise quadratically from the spectroscopic ionization potentials. The threshold for  $\text{Xe}^{3+}$  was found to rise as a cubic. The threshold for  $\text{Kr}^{3+}$  did not follow a cubic, however, as might be expected from the poor signal-to-noise ratio. As a check of the thresholds, the square roots of the double-ionization cross sections and the cube roots of the triple-ionization cross sections are fit by linear least squares and extrapolated to the x-axis intercept. The thresholds mea-

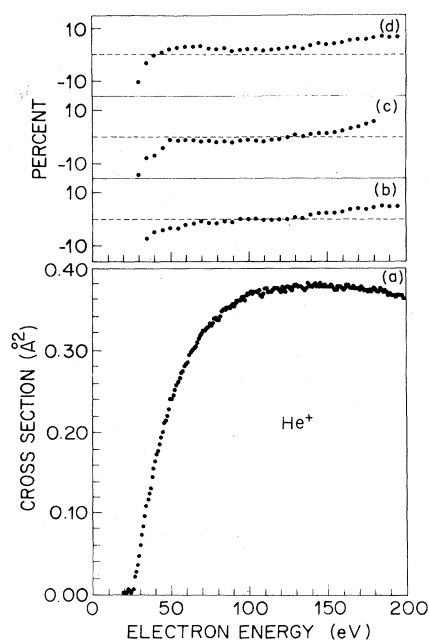


FIG. 12. (a) Absolute partial cross section for helium vs electron energy with comparisons to (b) Rapp and Englander-Golden (Ref. 15), (c) Stephan *et al.* (Ref. 20), and (d) Montague, Harrison, and Smith (Ref. 19).

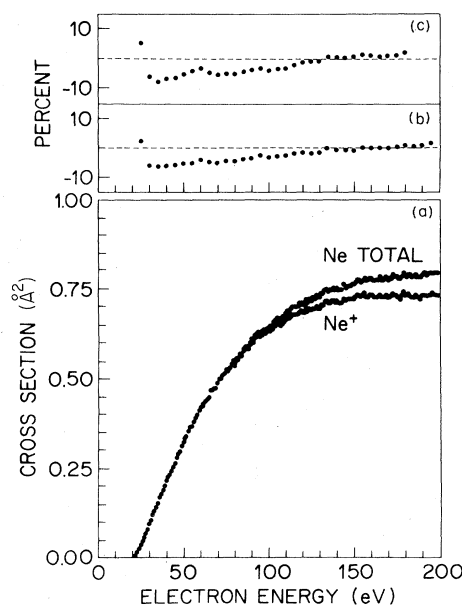


FIG. 13. (a) Absolute partial and total cross sections for neon vs electron energy with comparisons to (b) Rapp and Englander-Golden (Ref. 15), (c) Stephan *et al.* (Ref. 20).

TABLE IV. Absolute partial cross sections for electron-impact ionization of the rare-gas atoms to singly, doubly, and triply charged ions (in units of  $10^{-16} \text{ cm}^2$ ).

E (eV)	He <sup>+</sup>	Ne <sup>+</sup>	Ar <sup>+</sup>	Ar <sup>2+</sup>	$\sigma$ ( $10^{-16} \text{ cm}^2$ )		Kr <sup>3+</sup>	Xe <sup>+</sup>	Xe <sup>2+</sup>	Xe <sup>3+</sup>
					Kr <sup>+</sup>	Kr <sup>2+</sup>				
12								0.10		
13					0.01			0.31		
14					0.05			0.63		
15			0.00		0.18			1.00		
16			0.03		0.35			1.35		
17			0.15		0.56			1.65		
18		0.000	0.29		0.76			1.93		
19		0.000	0.44		0.96			2.17		
20	0.001	0.000	0.58		1.16			2.42		
21	0.002	0.002	0.71		1.33			2.67		
22	0.006	0.009	0.85		1.48			2.91		
23	0.005	0.019	0.96		1.65			3.12		
24	0.003	0.029	1.10		1.80			3.30		
25	0.008	0.037	1.25		1.96			3.46		
26	0.021	0.048	1.34		2.10			3.59		
27	0.028	0.062	1.44		2.27			3.73		
28	0.035	0.071	1.57		2.41			3.89		
29	0.047	0.081	1.68		2.49			4.04		
30	0.060	0.097	1.74		2.60			4.13	0.000	
31	0.072	0.108	1.86		2.70			4.23	0.000	
32	0.082	0.121	1.92		2.80			4.33	0.002	
33	0.095	0.135	2.02		2.89			4.43	0.004	
34	0.108	0.144	2.07		2.98			4.51	0.001	
35	0.117	0.151	2.20		3.08			4.59	0.008	
36	0.125	0.170	2.24		3.12			4.62	0.016	
37	0.132	0.179	2.31		3.17			4.67	0.016	
38	0.146	0.189	2.39		3.25			4.72	0.034	
39	0.156	0.204	2.42		3.30			4.74	0.046	
40	0.165	0.218	2.47	0.001	3.37	0.004		4.80	0.065	
45	0.201	0.266	2.56	0.003	3.50	0.025		4.82	0.157	
50	0.235	0.320	2.62	0.018	3.60	0.074		4.84	0.260	
55	0.261	0.371	2.62	0.040	3.65	0.130		4.86	0.323	
60	0.284	0.418	2.63	0.077	3.68	0.177		4.89	0.363	
65	0.302	0.454	2.63	0.108	3.69	0.214		4.93	0.377	
70	0.318	0.488	2.65	0.130	3.70	0.240		4.96	0.389	0.003
75	0.329	0.522	2.66	0.147	3.69	0.259		4.98	0.400	0.004
80	0.337	0.549	2.68	0.158	3.67	0.280		4.95	0.411	0.009
85	0.348	0.577	2.70	0.164	3.63	0.286		4.95	0.436	0.021
90	0.353	0.601	2.68	0.170	3.61	0.293	0.0022	4.92	0.456	0.033
95	0.360	0.623	2.67	0.171	3.57	0.300	0.0039	4.88	0.482	0.047
100	0.365	0.633	2.68	0.177	3.54	0.301	0.0066	4.84	0.510	0.065
105	0.369	0.650	2.67	0.176	3.51	0.301	0.0080	4.78	0.531	0.087
110	0.368	0.664	2.64	0.179	3.49	0.299	0.0105	4.77	0.545	0.109
115	0.370	0.679	2.63	0.180	3.46	0.298	0.0114	4.69	0.552	0.129
120	0.372	0.689	2.64	0.180	3.44	0.294	0.0134	4.63	0.553	0.147
125	0.373	0.694	2.61	0.177	3.42	0.291	0.0155	4.59	0.552	0.164
130	0.375	0.702	2.59	0.178	3.39	0.285	0.0175	4.55	0.542	0.174
135	0.374	0.714	2.57	0.175	3.37	0.283	0.0187	4.50	0.534	0.178
140	0.377	0.715	2.56	0.177	3.34	0.277	0.0202	4.46	0.525	0.182
145	0.377	0.719	2.54	0.178	3.32	0.275	0.0213	4.44	0.504	0.186
150	0.375	0.724	2.54	0.171	3.28	0.271	0.0224	4.38	0.494	0.186
155	0.374	0.731	2.53	0.171	3.26	0.269	0.0232	4.33	0.477	0.180
160	0.373	0.731	2.50	0.171	3.25	0.264	0.0235	4.30	0.467	0.179
165	0.375	0.728	2.48	0.169	3.22	0.258	0.0256	4.26	0.458	0.175
170	0.373	0.730	2.47	0.168	3.21	0.252	0.0257	4.24	0.446	0.170
175	0.371	0.731	2.44	0.163	3.16	0.251	0.0268	4.19	0.434	0.169
180	0.371	0.735	2.45	0.160	3.16	0.249	0.0270	4.16	0.426	0.166
185	0.371	0.731	2.42	0.158	3.12	0.245	0.0275	4.12	0.413	0.162
190	0.366	0.731	2.40	0.160	3.10	0.243	0.0285	4.08	0.406	0.160
195	0.364	0.734	2.39	0.157	3.08	0.238	0.0288	4.05	0.394	0.155
200	0.366	0.725	2.32	0.153	3.04	0.233	0.0307	4.03	0.391	0.156

TABLE V. Measured threshold energies (eV).

	Spectroscopic <sup>a</sup>	This work	REG <sup>b</sup>	SHM <sup>c</sup>
He <sup>+</sup>	24.59	24.56	24.57	24.33
Ne <sup>+</sup>	21.56	21.50	21.86	22.22
Ar <sup>+</sup>	15.76	15.82	16.06	15.30
Kr <sup>+</sup>	14.00	13.99	14.25	13.59
Xe <sup>+</sup>	12.13	12.03	12.19	
Ar <sup>2+</sup>	43.39	41.8		
Kr <sup>2+</sup>	38.36	38.2		
Xe <sup>2+</sup>	33.34	32.7		
Kr <sup>3+</sup>	75.31	69.2		
Xe <sup>3+</sup>	65.46	62.9		

<sup>a</sup>Reference 56.<sup>b</sup>Reference 15.<sup>c</sup>Reference 20.

sured in this way (Table V) lie acceptably close to the spectroscopic values, considering the noise near threshold and the extreme sensitivity of these fits to the choice of the baseline. Similar fits of the data of SHM are not meaningful because they reported points only every 5 eV.

### C. Cross-section shapes

The electron-energy dependence of the cross section is determined by scanning from 0 to 200 eV in 1 eV steps. Four signals are measured at each energy: electron-

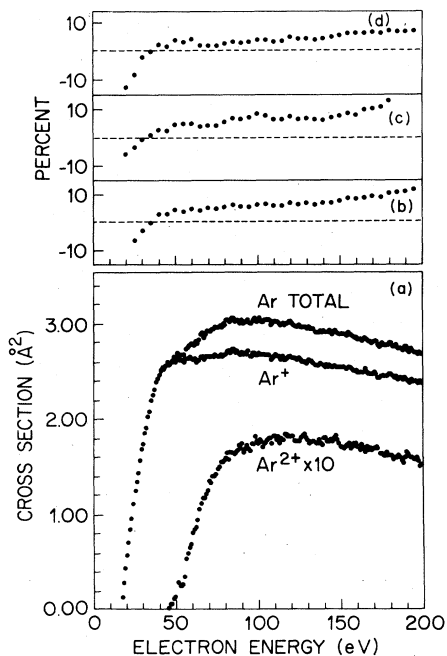


FIG. 14. (a) Absolute partial and total cross sections for argon vs electron energy with comparisons to (b) Rapp and Englander-Golden (Ref. 15), (c) Stephan *et al.* (Ref. 20), and (d) Kurepa *et al.* (Ref. 16).

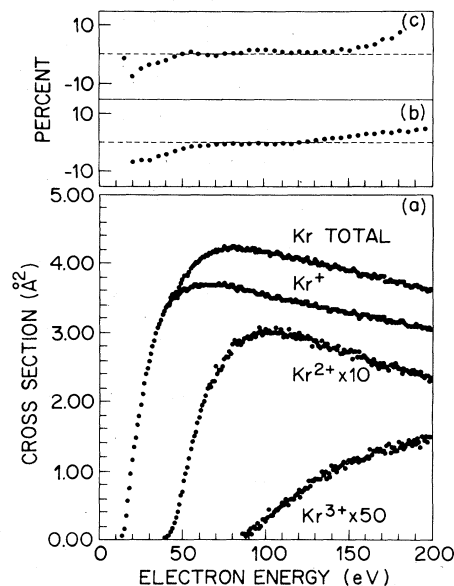


FIG. 15. (a) Absolute partial and total cross sections for krypton vs electron energy with comparisons to (b) Rapp and Englander-Golden (Ref. 15), (c) Stephan *et al.* (Ref. 20).

impact ion signal plus collisional ionization signal (electron gun on), collisional ionization signal (electron gun off), the electron current, and the neutral-beam flux (as monitored by  $I_{sec}$ ). The electron-impact ion signal (electron gun on minus off) is divided by the electron current and neutral flux at each energy to yield the “normalized”

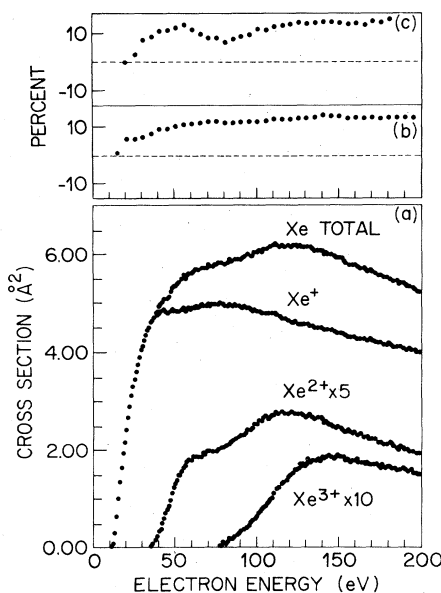


FIG. 16. (a) Absolute partial and total cross sections for xenon vs electron energy with comparison to (b) Rapp and Englander-Golden (Ref. 15), and (c) Stephan and Märk (Ref. 22).



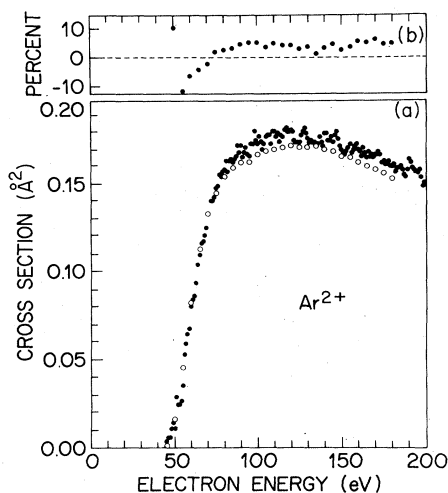


FIG. 17. (a) Partial cross section for  $\text{Ar}^{2+}$  measured in this work (solid circles) and that reported by Stephan *et al.* (Ref. 20). (b) Percent difference between the two measurements.

signal. This procedure corrects for systematic variation of electron current with electron energy, and for long term drifts in the neutral-beam intensity. Repetitive scans are added from 1 to 8 h, depending on the signal-to-noise ratio.

Shapes of the cross sections for single, double, and triple ionization are shown in Figs. 12–21 and in Table IV, where averages over 5 points are given for energies above 40 eV. The single-ionization shapes have been normalized to our absolute measurements. The multiple-ionization curves are normalized to the single-ionization curves by our measured ratios. Total ionization cross sections are then calculated from the values in Table IV, and are included in Figs. 12–16. The  $\text{He}^{2+}$  and  $\text{Ne}^{2+}$  contributions

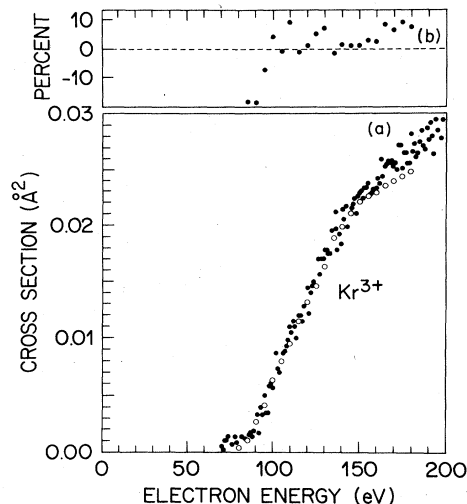


FIG. 19. (a) Partial cross section for  $\text{Kr}^{3+}$  measured in this work (solid circles) and that reported by Stephan *et al.* (Ref. 20). (b) Percent difference between the two measurements.

to the total cross section are small but not quite negligible, so we have taken the values from SHM.<sup>20</sup> For Ar, the data of SHM show that  $\sigma^{3+}$  is small enough to be neglected.

A sensitive measure of the agreement between these shapes and those of others is to plot the percent difference as a function of electron energy. For single and total ionization, these plots are included in Figs. 12–16 and show (absolute) agreement within  $\pm 15\%$  over the entire energy range. Comparison of our multiple-ionization data to that of SHM (Refs. 20 and 22) in Figs. 17–21 shows agreement within 15%, except near threshold of  $\text{Kr}^{2+}$ , and for Xe, where a 12% increase of SHM's cross sections would

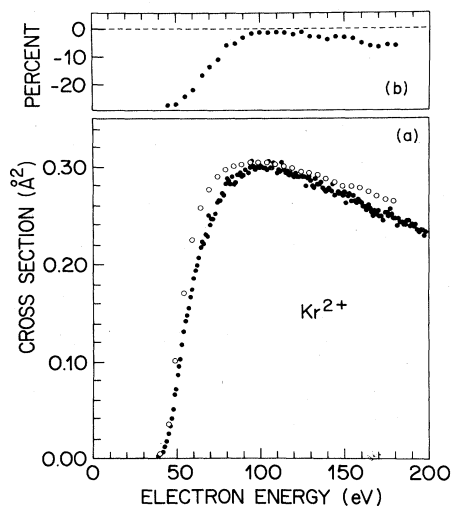


FIG. 18. (a) Partial cross section for  $\text{Kr}^{2+}$  measured in this work (solid circles) and that reported by Stephan *et al.* (Ref. 20). (b) Percent difference between the two measurements.

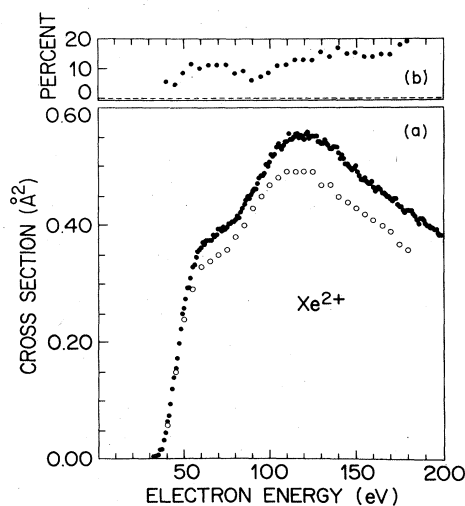


FIG. 20. (a) Partial cross section for  $\text{Xe}^{2+}$  measured in this work (solid circles) and that reported by Stephan and Märk (Ref. 22). (b) Percent difference between the two measurements.

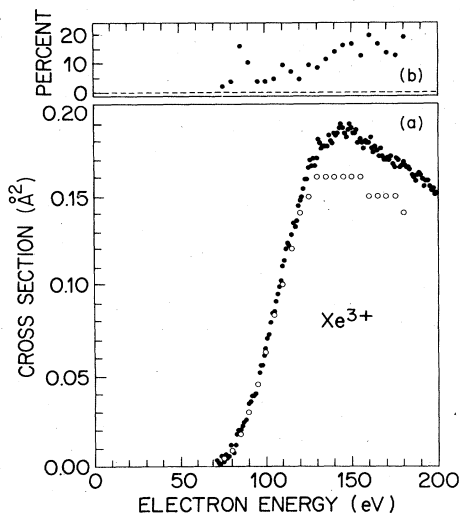


FIG. 21. (a) Partial cross section for  $\text{Xe}^{3+}$  measured in this work (solid circles) and that reported by Stephan and Märk (Ref. 22). (b) Percent difference between the two measurements.

improve the agreement greatly.

It appears that our cross sections are systematically low by several percent at energies below 50 eV and systematically high above 150 eV. The shape agreement among the other five workers makes it clear that the errors are in our data, probably related to our electron gun. It is likely that the overlap factor  $F$  varies with electron energy whereas we have taken it as a constant in the shape measurements. Also, the electron reflection correction  $\eta$  is expected to vary with energy, but our analysis treats it as a constant, since the literature measurements of  $\eta$  are insufficiently detailed. Correct treatment of these two effects should give more accurate shapes. Because the error is so reproducible and invariant for all five rare gases, an ad hoc correction to our future measurements would be to generate a correction function from the percent difference results of Figs. 12–21. Multiplication of the shapes measured with our present electron gun by

$$1.102 - 2.52 \times 10^{-3}E + 2.04 \times 10^{-5}E^2 - 5.91 \times 10^{-8}E^3 \quad (15)$$

gives the appropriately corrected shapes.

The amount of structure in the shape of the  $\text{Ar}^+$  curve has been controversial in recent years. Crowe, Preston, and McConkey<sup>52</sup> reported structure which they ascribed to autoionization, but which disagreed with many previous measurements. SHM's (Ref. 20) recent measurement confirmed the structure reported by Crowe *et al.*,<sup>52</sup> and agreed with the shape within a few percent. Our measurement also finds the same structure, and as shown in Fig. 14(c), agrees with the shape of SHM within a few percent, except for the systematic difference described by Eq. (15).

## V. CONCLUSIONS

One of the purposes of this paper is to describe our apparatus and assess its measurement accuracy. Analysis of the systematic errors gives 12%; combined with random errors from 5 to 11%, this gives about 15% overall uncertainty for absolute cross-section measurements. Clearly the agreement of our measured total cross sections with previous work is better, being within 6% for He, Ne, Ar, and Kr. This suggests that either our estimated uncertainties are too large, particularly for electron reflection, overlap, and CEM efficiency which have the largest uncertainties, or the errors in their values cancel fortuitously. We have, however, no *a priori* basis for claiming smaller uncertainties than those given in Table I. In the absence of more accurate measurements of  $\eta$ ,  $F$ , and  $\epsilon$  we could take another point of view, namely to normalize our results to the results of REG (omitting Xe). This would provide a value for the product  $\epsilon_1\epsilon_2\epsilon_3(1 + 1.60\eta)F$  almost identical to that we have used, but would give a rationale for reducing our estimated uncertainty from 15 to about 6%. The accuracy of our measured cross-section shapes appears to be in error by several percent at low and high energies. This shows up in the comparisons of our results to those of REG,<sup>15</sup> SHM,<sup>20</sup> and Montague *et al.*,<sup>19</sup> those results agree with each other to within about 2%, whereas we disagree by up to 6% at low and high energies. In the absence of improvements to the apparatus, we can correct this source of error in future measurements with an empirical correction function [Eq. (15)].

With these new absolute measurements available, we can reconsider the ionization cross sections for the rare gases. This is of particular importance since the rare gases are usually taken as the benchmarks or as the standards for normalization of other measurements. It is clear from Table III that our measurements confirm those of REG,<sup>15</sup> Montague *et al.*,<sup>19</sup> Kurepa *et al.*,<sup>16</sup> and Fletcher and Cowling,<sup>17</sup> although with our 15% absolute accuracy, this is not a stringent test. The 6% agreement of our He, Ne, Ar, and Kr cross sections with the previous values (Table III) suggests that for Xe, our 12% disagreement with REG is significant. Because there are reasons to question the REG value for Xe, we suggest that the Xe cross section be taken as the value reported here, namely a 12% increase over REG's value. The agreement between our measurements of multiple to single-ionization ratios and those of SHM (Ref. 20) suggests that for the first time after many decades of measurements, these ratios are now well known.

## ACKNOWLEDGMENTS

Dr. S. M. Tarr and Professor P. B. Armentrout were instrumental in the early development of this apparatus. Dr. L. H. Dubois, Dr. R. A. Gottscho, and Dr. J. M. Phillips provided valuable ideas and suggestions. We thank Dr. A. S. Schlachter for design details of the pyroelectric detector.

- <sup>1</sup>T. D. Märk, *Int. J. Mass Spectrom. Ion Phys.* **45**, 125 (1982).
- <sup>2</sup>T. M. Märk, in *Electron-Molecule Interactions and Their Applications*, edited by L. G. Christophorou (Academic, New York, 1984), Vol. 1, p. 251.
- <sup>3</sup>J. R. Peterson, in *Atomic Collision Processes*, Proceedings of the Third International Conference on the Physics of Electronic and Atomic Collisions, London, 1963, edited by M. R. C. McDowell (North-Holland, Amsterdam, 1964), p. 465; (private communication) as quoted by Ref. 18.
- <sup>4</sup>M. F. A. Harrison, *Brit. J. Appl. Phys.* **17**, 371 (1966).
- <sup>5</sup>A. J. Dixon, M. F. A. Harrison, and A. C. H. Smith, *J. Phys. B* **9**, 2617 (1976); P. R. Woodruff, M.-C. Hublet, and M. F. A. Harrison, *ibid.* **11**, L305 (1978); R. G. Montague, M. J. Diserens, and M. F. A. Harrison, *ibid.* **17**, 2085 (1984).
- <sup>6</sup>E. Brook, M. F. A. Harrison, and A. C. H. Smith, *J. Phys. B* **11**, 3115 (1978).
- <sup>7</sup>D. L. Ziegler, J. H. Newman, K. A. Smith, and R. F. Stebbings, *Planet. Space Sci.* **30**, 451 (1982); D. L. Ziegler, J. H. Newman, L. N. Goeller, K. A. Smith, and R. F. Stebbings, *ibid.* **30**, 1269 (1982).
- <sup>8</sup>P. B. Armentrout, S. M. Tarr, A. Dori, and R. S. Freund, *J. Chem. Phys.* **75**, 2786 (1981).
- <sup>9</sup>F. A. Baiocchi, R. C. Wetzel, and R. S. Freund, *Bull. Am. Phys. Soc.* **29**, 144 (1984); **29**, 804 (1984); R. C. Wetzel, F. A. Baiocchi, and R. S. Freund, *ibid.* **29**, 400 (1984); R. C. Wetzel, F. A. Baiocchi, T. R. Hayes, and R. S. Freund, *ibid.* **30**, 868 (1985).
- <sup>10</sup>F. A. Baiocchi, R. C. Wetzel, and R. S. Freund, *Phys. Rev. Lett.* **53**, 771 (1984).
- <sup>11</sup>T. R. Hayes, R. C. Wetzel, and R. S. Freund, *Proceedings of the Fourteenth International Conference on the Physics of Electronic and Atomic Collisions, Palo Alto, 1985*, edited by M. J. Coggiola, D. L. Huestis, and R. P. Saxon (ICPEAC, Palo Alto, 1985), p. 161.
- <sup>12</sup>L. J. Kieffer and G. H. Dunn, *Rev. Mod. Phys.* **38**, 1 (1966).
- <sup>13</sup>T. D. Märk, *Beitr. Plasmaphys.* **22**, 257 (1982).
- <sup>14</sup>P. T. Smith, *Phys. Rev.* **36**, 1293 (1930).
- <sup>15</sup>D. Rapp and P. Englander-Golden, *J. Chem. Phys.* **43**, 1464 (1965).
- <sup>16</sup>M. V. Kurepa, I. M. Čadež, and V. M. Pejčev, *Fizika (Zagreb)* **6**, 185 (1974).
- <sup>17</sup>J. Fletcher and I. R. Cowling, *J. Phys. B* **6**, L258 (1973).
- <sup>18</sup>P. Nagy, A. Skutlartz, and V. Schmidt, *J. Phys. B* **13**, 1249 (1980).
- <sup>19</sup>R. G. Montague, M. F. A. Harrison, and A. C. H. Smith, *J. Phys. B* **17**, 3295 (1984).
- <sup>20</sup>K. Stephan, H. Helm, and T. D. Märk, *J. Chem. Phys.* **73**, 3763 (1980).
- <sup>21</sup>F. Egger and T. D. Märk, *Z. Naturforsch. Teil A* **33**, 1111 (1978).
- <sup>22</sup>K. Stephan and T. D. Märk, *J. Chem. Phys.* **81**, 3116 (1984).
- <sup>23</sup>L. Wahlin, *Nucl. Instrum. Methods* **27**, 55 (1964).
- <sup>24</sup>J. B. Hasted, *Physics of Atomic Collisions* (Butterworth, London, 1964).
- <sup>25</sup>A. S. Schlachter, K. R. Stalder, and J. W. Stearns, *Phys. Rev. A* **22**, 2494 (1980); R. H. McFarland, A. S. Schlachter, J. W. Stearns, B. Liu, and R. E. Olson, *ibid.* **26**, 775 (1982); K. H. Berkner, B. R. Meyers, and R. V. Pyle, *Rev. Sci. Instrum.* **39**, 1204 (1968); M. W. Geis, K. A. Smith, and R. D. Rundel, *J. Phys. E* **8**, 1011 (1975).
- <sup>26</sup>EDO Corporation, Western Division, 300 South State College Blvd, Fullerton, CA 92631.
- <sup>27</sup>T. A. Miller and R. S. Freund, *Adv. Magn. Reson.* **9**, 49 (1977).
- <sup>28</sup>P. O. Taylor, K. T. Dolder, W. E. Kauppila, and G. H. Dunn, *Rev. Sci. Instrum.* **45**, 538 (1974).
- <sup>29</sup>T. D. Märk and F. J. de Heer, *J. Phys. B* **12**, L429 (1979); M. F. A. Harrison, A. C. Smith, and E. Brook, *ibid.* **12**, L433 (1979).
- <sup>30</sup>D. W. O. Heddle, *Proc. Phys. Soc.* **90**, 81 (1967).
- <sup>31</sup>E. W. McDaniel, *Collision Phenomena in Ionized Gases* (Wiley, New York, 1964), p. 658.
- <sup>32</sup>O. Hachenberg and W. Brauer, *Adv. Electron. Electron Phys.* **11**, 413 (1959).
- <sup>33</sup>E. J. Sternglass, *Phys. Rev.* **95**, 345 (1954).
- <sup>34</sup>R. A. Langley, J. Bohdansky, W. Eckstein, P. Mioduszewski, J. Roth, E. Taglauer, E. W. Thomas, H. Verbeek, and K. L. Wilson, *Nucl. Fusion, Special Issue*, **9**, 94 (1984).
- <sup>35</sup>C. E. Kuyatt, J. A. Simpson, *Rev. Sci. Instrum.* **38**, 103 (1967).
- <sup>36</sup>R. D. Rundel, D. E. Nitz, K. A. Smith, M. W. Geis, and R. F. Stebbings, *Phys. Rev. A* **19**, 33 (1979).
- <sup>37</sup>C. Burrows, A. Lieber, and V. Zaviantseff, *Rev. Sci. Instrum.* **38**, 1477 (1967).
- <sup>38</sup>J. Fricke, A. Muller, and E. Salzborn, *Nucl. Instrum. Methods* **175**, 379 (1980).
- <sup>39</sup>J. P. Ravon, *Nucl. Instrum. Methods* **211**, 7 (1983).
- <sup>40</sup>D. Heschen, Galileo Electro-Optics Corporation (private communication).
- <sup>41</sup>P. Defrance, W. Claeys, A. Cornet, and G. Poulaert, *J. Phys. B* **14**, 111 (1981).
- <sup>42</sup>R. S. Freund, in *Rydberg States of Atoms and Molecules*, edited by R. F. Stebbings and F. B. Dunning (Cambridge University Press, Cambridge, 1982), p. 355.
- <sup>43</sup>W. Bleakney, *Phys. Rev.* **36**, 1303 (1930).
- <sup>44</sup>J. T. Tate and P. T. Smith, *Phys. Rev.* **46**, 773 (1934).
- <sup>45</sup>D. P. Stevenson and J. A. Hipple, *Phys. Rev.* **62**, 237 (1942).
- <sup>46</sup>R. E. Fox, *Advances in Mass Spectroscopy*, edited by S. D. Waldron (Pergamon, London, 1953), p. 397.
- <sup>47</sup>F. Fiquet-Fayard, *J. Chim. Phys.* **59**, 439 (1962); F. Fiquet-Fayard and M. Lahmani, *ibid.* **59**, 1050 (1962).
- <sup>48</sup>C. E. Melton and P. S. Rudolph, *J. Chem. Phys.* **47**, 1771 (1967).
- <sup>49</sup>A. Gaudin and R. Hagemann, *J. Chim. Phys.* **64**, 1209 (1967).
- <sup>50</sup>J. P. Ziesel, *J. Chim. Phys.* **64**, 695 (1967).
- <sup>51</sup>J. D. Morrison and J. C. Traeger, *J. Chem. Phys.* **53**, 4053 (1970).
- <sup>52</sup>A. Crowe, J. A. Preston, and J. W. McConkey, *J. Chem. Phys.* **57**, 1620 (1972).
- <sup>53</sup>H. J. Drewitz, *Int. J. Mass. Spectrom. Ion Phys.* **19**, 313 (1976); **21**, 212 (1976).
- <sup>54</sup>B. L. Schram, H. R. Moustafa, J. Schutten, and F. J. de Heer, *Physica* **32**, 734 (1966).
- <sup>55</sup>B. L. Schram, F. J. de Heer, M. J. van der Wiel, and J. Kistemaker, *Physica* **31**, 94 (1965).
- <sup>56</sup>R. E. Winters, J. H. Collins, and W. L. Courchene, *J. Chem. Phys.* **45**, 1931 (1966).
- <sup>57</sup>C. E. Moore, *Ionization Potentials and Ionization Limits Derived From the Analyses of Optical Spectra*, Natl. Stand. Ref. Data Ser., Natl. Stand. (U.S.) Circ. No. 34 (U.S. GPO, Washington, D.C., 1970).